

GeoLCR: Attention-based Geometric Loop Closure and Registration

Jing Liang¹, Sanghyun Son¹, Ming C. Lin¹ and Dinesh Manocha¹
<https://youtu.be/QdMu3-Rztcg>

Abstract—We present a novel algorithm for learning-based loop-closure for SLAM (simultaneous localization and mapping) applications. Our approach is designed for general 3D point cloud data, including those from lidar, and is used to prevent accumulated drift over time for autonomous driving. We voxelize the point clouds into coarse voxels and calculate the overlap to estimate if the vehicle drives in a loop. We perform point-level registration to compute the current pose accurately. We have evaluated our approach on well-known datasets KITTI [1], KITTI-360 [2], Nuscenes [3], Complex Urban [4], NCLT [5], and MulRan [6]. We show at most 2 times improvement in accuracy estimation of translation and rotation. On some challenging sequences, our method is the first approach that can obtain a 100% success rate of loop detection.

I. INTRODUCTION

Simultaneous localization and mapping (SLAM) is widely used in robotics and autonomous navigation applications [7], [8], [9], [10]. The goal of SLAM algorithms is to estimate the positions of the robot (or ego-vehicle) while traveling or navigating in an unknown environment while simultaneously building a map of the environment.

Current robots and autonomous vehicles use different sensors, including mono-Cam, RGBD camera, lidar, and IMU to guide navigation. As a result, different sets of perception algorithms have been developed for each of those sensors. Monocular cameras are very widely used in SLAM tasks [11]. The visual SLAM approach can also be optimized by using an IMU sensor. With the development of RGBD cameras, these algorithms can accurately compute the depth data, which can improve the accuracy of the map building. The lidar sensor is regarded as the most accurate and long-range sensor for depth information. Many approaches [8], [12], [10], [9] use lidars for mapping and localization. In practice, the quality of depth information computed using lidar sensors is better than RGBD sensors. In this paper, we mainly limit ourselves to using lidar as the primary perceptive sensor.

Overall, SLAM computation includes two major steps: (1) Local odometry to build a consistent map within a short distance [13], [8], [7]. However, local odometry

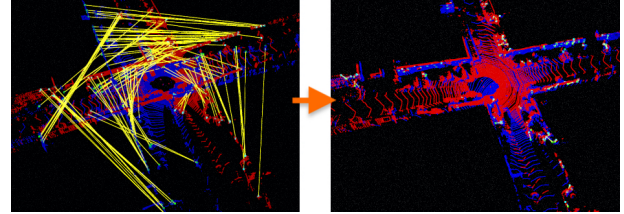


Fig. 1: The overlap estimation and registration when the car arrives a previous location in a cross. The yellow lines on the left represent the matched voxels and the right side is the map after registration.

tends to accumulate the drift over time. (2) Loop closure is applied when the robot runs into a closed loop and then rectifies the built map [14], [10], [9]. This is also used to overcome the problems with drift accumulation. In this paper, we mainly focus on loop closure, including detection of loop closure as well as pose computation.

As Figure 1, loop closure within SLAM computation consists of two sub-tasks: (a) Detect the closed loop scenario, where the robot needs to identify if the current environment is similar to any of the previous scenarios; (b) Recalculate the current position based on detected similar frames and rectify the map and trajectory to alleviate the drift accumulated during the local odometry tasks. ICP-based methods are frequently used [8], [12] as a traditional approach, but the optimization-based algorithms often suffer from local minimum issues. Most of the current learning-based approaches [9], [10] focus on autonomous cars that only requires yaw angle in registration and the points are long-range Lidar points with many channels. However, those cannot provide the distance related information nor can these methods be directly used by small robots that requires 3D rotation and translation with short-range of Lidar sensors.

Main Contributions: We present GeoLCR, a learning-based approach for geometric loop closure and point-level registration for both cars and small robots usages. Our formulation includes coarse matching and registration. We describe novel techniques for overlap and pose calculations to make our formulation more accurate. The novel components of our work include:

- 1) We propose an overlap detection metric for 3D loop closure detection. Based on the Geometric Transformer [15], we develop an overlap estimator to estimate the overlap values. We demonstrate

¹ Authors are from Computer Science Department, University of Maryland, College Park

Website: <https://gamma.umd.edu/researchdirections/autonomousdriving/geolcr/>
 Code: <https://github.com/jingGM/GeoLCR.git>

that the overlap estimation is consistent with the distances between two point clouds and easy to use for loop closure detection.

- 2) We propose a novel transformer-based registration model that is specific for our overlap estimator. This model only takes the points in matched voxels from the previous overlap estimator. We exploit the fact that the distance between coarse features corresponds to the overlap between a pair of voxels and take these features into account to improve the accuracy of point matching. We also show that our registration transformer generates better results (see Section IV) and the appendix [16].
- 3) We demonstrate the efficacy of our approach using different datasets, including those based on cars and small robots. We evaluate the accuracy and performance of our method on KITTI [1], KITTI-360 [2], Nuscenes [3], Complex Urban [4], NCLT [5] and MulRan [6]. We show that our approach is up to two times more accurate in registration and also more accurate in overlap detection than other state-of-the-art methods [16].

II. BACKGROUND

Different techniques have been proposed for loop closure based on the underlying sensors. In terms of camera-based and lidar-based approaches, there are many traditional approaches as well as learning-based approaches [17], [9], [10]. In this section, we mainly limit ourselves to techniques proposed for lidar sensors.

A. Loop Closure Detection

The traditional loop closure algorithms using lidar data are mostly based on optimization approaches [8], [7], where the Levenberg-Marquardt algorithm is used to find the minimum distance between the point clouds directly [7], [18]. The Lio-sam [12] algorithm uses an extra GPS sensor and introduces the GPS graph factor to help with the detection of loop closure. LLoam [19] segments the lidar data and builds a factor graph to perform graph optimization for loop closure detection. LDSO [20] uses the image features to build a similar bag-of-words (BoW) approach and uses a sliding window to perform optimization. However, those approaches suffer from local minimum problems, where the current pose estimation may not be accurate.

With the development of learning-based approaches, researchers are able to extract the semantic information from point clouds and compare the semantic features from different frames for loop closure. Lin et al. [21] use the semantic information to build a topology graph and compare the objects' relative positions within two frames; SA-LOAM [22] extracts the semantic information of each sub-graph (i.e. the local map) and then

compares the similarity of the sub-graphs for loop closure. [23] uses a similar approach to generate local map descriptors and compare the likelihood of the descriptors. Although these semantic approaches can compute the similarities of different local frames, they cannot predict the overlap or matching of different local frames. Recently, several approaches have been proposed that can directly predict the overlap between the local frames [10], [24], [25], [9]. However, their predictions are based on the 2D birds-eye-view graph, and they directly use the overall point cloud for registration, which can be computationally expensive and requires a lot of storage. In this paper, we present a new method based on a geometric transformer to predict the overlap and use the points in matched voxels to perform points registration and predict the current position.

B. Point Registration and Map Rectification

After detecting the loop closure, a new estimate of the current position needs to be predicted with the matched frame. There are many known approaches that can be used for point registration. Traditionally, researchers have used ICP/GICP [13] for registration with the help of RANdom SAMple Consensus (RANSAC). For learning-based approaches, the Sinkhorn algorithm and differentiable Singular Value Decomposition (SVD) approaches have been combined for the registration task [15], [10]. These approaches take into account all the points for calculation, which can be computationally costly and subject to local minima issues. We present a novel approach using a point transformer that takes the features of matched voxels for registration and estimates the transformation matrix between the points in matched pairs to reduce the computation.

For map rectification, prior methods mainly use key frames to detect loop closure and modify the map by spreading the detected error of the current position to all the previous key frames in the loop [8], [18]. However, those key frames may not be the closest frame to the current frame, which can impact the effectiveness of map modification. The Elastic Fusion [14] algorithm uses a non-rigid map rectification by adjusting the map based on neighbors of the changed frames. However, in the real world scenarios, different frames may have different errors in terms of frame estimation. In this work, Lio-sam [12] is used as the high-frequent odometry and use factor graphs to rectify the map in closed loops.

III. APPROACH

In this section, we give the definition of the overlap and describe the details of the overlap and registration models. In this project, we use 3D Lidar as the primary sensor for observation, and the observed data are points $\mathbf{p} \in \mathbb{R}^3$. We focus on the loop closure task, which

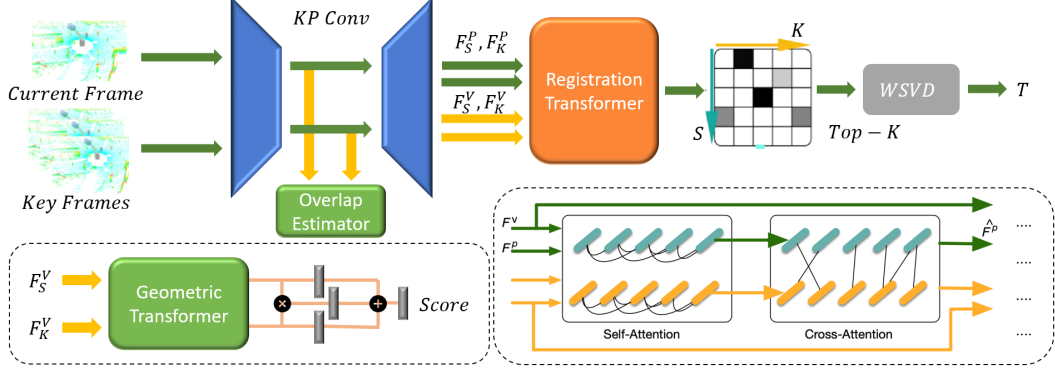


Fig. 2: **Overlap estimation and point registration pipeline:** For a given current frame and the key frames recorded in the past, we use KPConv [26] to extract point and voxel features hierarchically. We take the voxel features to estimate the overlap score by the Overlap Estimator. The voxel features are also used along with point features in estimating the relative poses in the Registration Transformer. The Registration model uses attention heads to estimate the matching relationship between the points before using this matching relationship to compute the final pose.

includes: First, estimate the overlaps between the current key frame s and the selected previous key frames; Second, predict the transformation matrix $T \in SE(3)$ between the current key frame s , and the overlapped historic key frame k .

In this approach, the inputs are two point clouds, \mathcal{P}_s from the current key frame s and \mathcal{P}_k from the historic key frame k , as shown in Figure 2. We first voxelize the points into the voxel clouds, \mathcal{Q}_s and \mathcal{Q}_k , respectively. Then these voxel clouds are processed in the following three-stage pipeline:

- 1) Feature extraction: A hierarchical feature extractor KPConv [26] is used to extract the features of both the points and the voxels, \mathcal{F}_p and \mathcal{F}_v ;
- 2) Overlap estimation: We estimate the overlap scores between the current key frame and the experienced key frames, and if an overlap score is higher than a threshold value, we consider the robot has closed the loop at the location of the corresponding historic key frame;
- 3) Registration: We estimate the transformation matrix T between the two frames.

A. Overlap Definition

For overlap detection, a sequence of keyframes is compared with the current frame of observation. For each frame, we use a voxelization method [27] to down-sample the point clouds corresponding to this frame. The position of each voxel is calculated by the mean value of all the points in the voxel using Equation 1:

$$\mathbf{v}_i = \frac{1}{|\mathcal{C}_i|} \sum_{\mathbf{p}_m \in \mathcal{C}_i} \mathbf{p}_m, \quad (1)$$

where position $\mathbf{v}_i \in \mathcal{Q}_s$ is the position of voxel i in the current key frame s , then we can also have $\mathbf{v}_j \in \mathcal{Q}_k$ as

the position of voxel j in one of the previous key frames k . \mathcal{Q}_s and \mathcal{Q}_k represent the voxel clouds generated from point clouds \mathcal{P}_s and \mathcal{P}_k frame s and k , respectively. All the points in the voxel space of voxel i compose the point set \mathcal{C}_i , so $\mathbf{p}_m \in \mathbb{R}^3$ represents the m_{th} point in \mathcal{C}_i . The overlap between the two voxel clouds of the current keyframe and a historic keyframe is given as

$$O(\mathcal{Q}_s, \mathcal{Q}_k) = \frac{\mathcal{M} \sum_{i,j} o_{i,j} \mathcal{I}_{i,j}}{\min\{|\mathcal{Q}_s|, |\mathcal{Q}_k|\}}, \quad (2)$$

$$\mathcal{I}_{i,j} = \begin{cases} 1, & \text{when } o_{i,j} > th \\ 0, & \text{otherwise} \end{cases} \quad (3)$$

where \mathcal{M} is the number of matched pairs of voxels in the two voxel clouds. $\mathcal{I}_{i,j} \in \{0, 1\}$ represents the indicator function that gives 1 when two voxels i and j overlap, where th is the threshold for the overlap score. In this project, we set $th = 0.1$. The $o_{i,j}$ represents the overlap score of one pair of voxels, i, j . We use the overlap estimator in Figure 2 to extract the overlap score. In the training stage, the ground truth for the overlap score is calculated as:

$$o_{i,j} = \exp \frac{-\sum_{\mathbf{p}_m \in \mathcal{C}_j} \|\mathbf{p}_m - \mathbf{p}_n\|_2}{|\mathcal{C}_j|}, \quad (4)$$

where $\mathbf{p}_m \in \mathcal{C}_j$ and $\mathbf{p}_n \in \mathcal{C}_i^T$, \mathcal{C}_i and \mathcal{C}_j are point sets of voxels i and j in frames s and k . \mathcal{C}_i^T is the transformed point set of \mathcal{C}_i by the ground-truth transformation matrix T (Figure 2), and \mathbf{p}_n is the nearest point in \mathcal{C}_i^T to \mathbf{p}_m . In implementation, when the overlap score $O(\mathcal{Q}_s, \mathcal{Q}_k) > 0.5$, we consider the two key frames overlapped.

B. Overlap Estimation

For overlap estimation, we use the voxels' features and positions to estimate the matched pairs. To be specific, we leveraged Geometric Transformer [15] for

the estimation, but it cannot estimate the overlap score of each pair of matched voxels. Therefore, we developed the overlap estimator in Figure 2 to calculate the overlap score for each pair of voxels.

The voxel features computed from Geometric Transformer [15] are \mathbf{f}^s and \mathbf{f}^k , which are from the current key frame s and one historic key frame k and they are normalized features. From the features, we can get the feature similarity as:

$$\hat{d}(\mathbf{f}_i^s, \mathbf{f}_j^k) = 1 - \|\mathbf{f}_i^s - \mathbf{f}_j^k\|_2. \quad (5)$$

And we can estimate the overlap score as:

$$\hat{o}(\mathbf{f}_i^s, \mathbf{f}_j^k) = \text{sigmoid}[g(h_s(\mathbf{f}_i^s) + h_c(\mathbf{f}_i^s \cdot \mathbf{f}_j^k) + h_k(\mathbf{f}_j^k))]$$

where $g(\cdot)$, $h_s(\cdot)$, $h_c(\cdot)$, and $h_k(\cdot)$ all contain a sequence of linear layers with ReLU activation function. In this project, we found two linear layers are good enough for $g(\cdot)$, $h_s(\cdot)$, $h_c(\cdot)$, and $h_k(\cdot)$. The details of the networks are in supplement materials [16].

The loss function of the whole overlap estimation model has two parts: the first part is similar to the circle loss [15] and the second part is used for accurate overlap estimation. In the following equations, we use $o_{i,j}$ for the ground truth of the overlap score between the two voxels i and j , $\hat{o}_{i,j}$ for the estimation, and $\hat{d}_{i,j} \in [0, 1]$ for the feature similarity $\hat{d}(\mathbf{f}_i^s, \mathbf{f}_j^k)$.

$$\mathcal{L}_i = \mathcal{L}_i(s) + \mathcal{L}_i(k) \quad \text{where} \quad \mathcal{L}_i = \alpha \mathcal{L}_i^p + \beta \mathcal{L}_i^n; \quad (6)$$

$$\mathcal{L}_i^p = \frac{1}{|\mathcal{P}|} \text{LSE}(\mathcal{I}_{i,j}(\hat{d}_{i,j} - \mathcal{I}_{i,j})^2); \quad (i, j) \in \mathcal{P} \quad (7)$$

$$\mathcal{L}_i^n = \frac{1}{|\mathcal{N}|} \text{LSE}((0 - \hat{d}_{i,j})^2); \quad (i, j) \in \mathcal{N} \quad (8)$$

where \mathcal{L}_i is the total circle loss [15] and the $\mathcal{L}_i(s)$ and $\mathcal{L}_i(k)$ represent the circle loss for the voxels in current key frame s and the historic key frame k , respectively. Each \mathcal{L}_i contains two loss functions \mathcal{L}_i^p and \mathcal{L}_i^n . \mathcal{L}_i^p is the loss for overlapped pairs, as in Equation 7, where \mathcal{P} represents the set of overlapped voxel pairs. \mathcal{L}_i^n is the loss for non-overlapping pairs, as in Equation 8, where \mathcal{N} represents the voxel pairs with no overlapping areas. LSE is the LogSumExp loss. α and β are all hyper-parameters.

The loss for the overlap values is \mathcal{L}_o , where MSE represents the mean squared error and $\hat{O} = \{\hat{o}_{i,j}\}$ and $O = \{o_{i,j}\}$ are estimated and real overlap values for all pairs of voxels i, j in the two frames s and k :

$$\mathcal{L}_o = \text{MSE}(\hat{O} - O) \quad (9)$$

The total loss of the overlap estimation is $\mathcal{L}_c = \mathcal{L}_o + \mathcal{L}_i$. Next, we calculate the overlap of the matched frames based on Equation 3. If the keyframe and the current frame satisfy the overlapped criteria, those matched voxels are used for point registration.

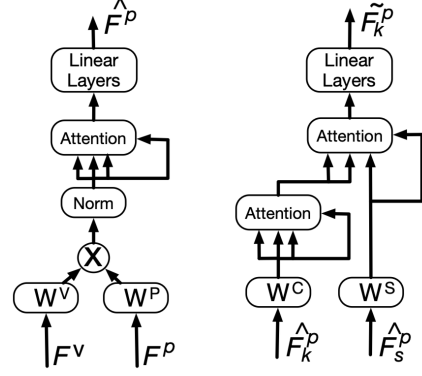


Fig. 3: **Attention-based registration:** The registration model includes self-attention (left) and cross-attention (right) models in sequence. The voxel features \mathcal{F}^v and point features \mathcal{F}^p from two frames are inputs of the self-attention model and cross-attention model takes the output of the self-attention model to process the relationship between two frames of points. The final point features are used to compute the weights for the weighted SVD approach, as defined in Equation 12.

C. Point Registration

In this section, we describe our novel method for point registration to generate the transformation matrix between two key frames. Since we only use Lidar as the perceptive sensor, if the point clouds do not overlap much or are in very different shapes, it would be hard to estimate the accurate transformation matrix between them. Therefore, rather than using whole point clouds, we only choose the points from highly overlapped voxel pairs and leverage their matching relationships.

After the voxel matching step, we have the matched pairs of voxels $\{i, j\}$ with corresponding point sets \mathcal{C}_i and \mathcal{C}_j as the input of the registration step. As shown in Figure 2, the registration step includes a Registration Transformer model and a WSVD (weighted SVD) model [28]. First, we do point matching by the Registration Transformer model, which computes matching scores for each pair of points in the selected voxel pairs. Then the points features are processed by the WSVD model to generate the transformation matrix T .

For the Registration Transformer, instead of only using the points in the registration task, as Figure 3 shows, we take advantage of the features of the matched voxels \mathcal{F}^v , where $\mathbf{f}_i^s, \mathbf{f}_j^k \in \mathcal{F}^v$, to help with point matching. As shown in Figure 3, \mathcal{F}^p represents the features of points. We first project the processed voxel features, $W^v \mathcal{F}^v$, to the space of processed point features, $W^p \mathcal{F}^p$, where W^v and W^p are weights for the features of voxels and points. After normalization, we put the features to the attention networks then post-process the features by several linear layers. The entire process of the self-attention model $k_{self}(\cdot)$ is on the left. Our attention model is based on

the multi-head attention model [29]. The output of the self-attention model is $\hat{\mathcal{F}}^p$, as :

$$\hat{\mathcal{F}}^p = k_{self}(\mathcal{F}^v, \mathcal{F}^p) \quad (10)$$

Then we pass the results to the cross-attention model $k_{cross}(\cdot)$. To be specific, after we process both s and k frames by self-attention module and generate $\hat{\mathcal{F}}_s^p$ and $\hat{\mathcal{F}}_k^p$, the cross-attention model takes them as inputs. W^c and W^s correspond to the weights of the inputs and the corresponding cross-attention output features of the points are $\tilde{\mathcal{F}}_s^p$ and $\tilde{\mathcal{F}}_k^p$. All these features have the shape of $v \times p \times d$, where v is the size of matched voxels, p is the size of points in each voxel, and d is the feature dimension.

$$\tilde{\mathcal{F}}_k^p = k_{cross}(\hat{\mathcal{F}}_s^p, \hat{\mathcal{F}}_k^p), \quad \tilde{\mathcal{F}}_s^p = k_{cross}(\hat{\mathcal{F}}_k^p, \hat{\mathcal{F}}_s^p) \quad (11)$$

We use the Einstein sum to calculate the matching scores between two points features:

$$s[a, m, n] = \sum_{k \in \{0, \dots, d\}} \hat{\mathcal{F}}_k^p[a, m, k] \times \hat{\mathcal{F}}_s^p[a, n, k] \quad (12)$$

where $a \in [0, v)$ is the index of matched voxel pairs. $m \in [0, |\mathcal{C}_i|)$ and $n \in [0, |\mathcal{C}_j|)$ are the indices of the points from the point sets \mathcal{C}_i and \mathcal{C}_j of the overlapped voxels i and j . Then we have the score map with the shape $(v, |\mathcal{C}_i|, |\mathcal{C}_j|)$. We choose the points with the biggest value in the last dimension to compose the point pairs with the score map s , which now has the shape of $(v, |\mathcal{C}_i|)$. Those scores are used as weights for the point pairs to be put into the differentiable weighted SVD model [28].

The loss function of the registration stage contains two parts: The first part aims at reducing the error of the estimated transformation matrix. Inspired by the transformation loss [30], the first part of the loss function is given as:

$$\mathcal{L}_{matrix} = \left\| \hat{R}^T R_g - I \right\|_2^2 + \left\| \hat{t} - t_g \right\|_2^2$$

where \hat{R} and \hat{t} are the estimated rotation and translation transformations, and the estimated transformation matrix \hat{T} is composed of \hat{R} and \hat{t} . I is a (3×3) identity matrix. R_g and t_g are the ground truth transformations corresponding to rotation and translation.

The second part is aimed at reducing the distances between the two transformed point clouds $\hat{T}\mathbf{p}_s$ and $T_g\mathbf{p}_s$, where \hat{T} and T_g represent the estimated transformation matrix and the ground truth transformation matrix:

$$\mathcal{L}_{distance} = \text{MSE}(\hat{T}\mathbf{p}_s - T_g\mathbf{p}_s), \quad (13)$$

The total loss for the registration stage is given as:

$$\mathcal{L}_r = \gamma \mathcal{L}_{matrix} + \eta \mathcal{L}_{distance}, \quad (14)$$

where γ and η are coefficients. This loss function is for the points registration. In the training phase, we combine the overlap loss function and registration loss function together $\mathcal{L} = \mathcal{L}_c + \mathcal{L}_r$ for the whole training.

D. Loop Closure and Odometry

Algorithm 1 Loop Closure. The low level odometry is implemented by Lio-sam, and the following is the loop closure detection and loop constraints publication. $N = 2$ in this project.

Require: \mathbf{f}_c the current frame

Require: \mathcal{K} the set of previous keyframes in sequence

```

1: procedure LOOP CLOSURE
2:    $\mathcal{K}_n \leftarrow \text{RemoveFarFrames}(\mathcal{K}, \mathbf{f}_c)$ 
3:   for  $\mathbf{f}_k \leftarrow \mathcal{K}_n$  do
4:      $O(\mathcal{O}_s, \mathcal{O}_k) \leftarrow \text{OverlapEstimator}$ 
5:     if  $O(\mathcal{O}_s, \mathcal{O}_k) > O_{th}$  then
6:        $\hat{T} \leftarrow \text{PointRegistration}(\mathbf{f}_s, \mathbf{f}_k)$ 
7:       if  $\hat{T}.translation < \mathbf{d}_{th}$  then
8:         PublishLoopConstraints
9:       end if
10:    end if
11:  end for
12:  add  $\mathbf{f}_c$  to  $\mathcal{K}$  each N frames.
13: end procedure

```

The low-level odometry is achieved by Lio-sam [12], which is based on GTSAM [31]. The map modification is done by the factor graph [31] method. As shown in Algorithm 1, when a robot is moving, our model gets the frames from Lio-sam and saves each key frame \mathbf{f}_c from every N received frames, where N is 2 in this project.

The *RemoveFarFrames* function removes the historic key frames far from the current key frame. The distance threshold is set as 5 meters. This function also removes the frames, \mathcal{H}_c , in the last 10 meters of the trajectory from the current key frame \mathbf{f}_c . For all saved key frames \mathbf{f}_k , we have the constraints:

$$\mathbf{f}_k \notin \mathcal{H}_c \text{ and } \|\mathbf{f}_k - \mathbf{f}_c\|_2 < 5 \quad (15)$$

The *OverlapEstimator* is our Overlap Estimator model, which predicts the overlap value between the two point clouds, and the *PointRegistration* is the registration model, which estimates the transformation matrix between the two point clouds.

Given the transformation matrix, if the translation value is smaller than the threshold $\mathbf{d}_{th} = 3m$, we consider the loop closed. The loop constraints include the transformation matrix and the timestamps of the two frames. *PublishLoopConstraints* function publishes all the loop constraints to the low-level odometry, Lio-sam, for map rectification.

Methods	Feature Extract[ms]	Registration[ms]	Total[ms]
OverlapNet	16.00	6.00	38.00
RPMNet	366.75	121.29	854.79
DCP	187.71	80.77	456.18
LCDNet	94.60	1135	1324.2
Ours	500	97	597
Ours(CUDA)	200	97	297

TABLE I: From the table we can see our models run very fast. Although our data preprocessing takes time, the total computational time is still low.

IV. RESULTS AND COMPARISONS

To validate our approach, we tested our method on KITTI [1], KITTI-360 [2], datasets. We compared the accuracy of our pose estimation results and map rectification results with other state-of-the-art methods, including OverlapNet [9] and LCDNet [10]. For more comparisons with different datasets (Nuscenes [3], Complex Urban [4], NCLT [5] and MulRan [6]) and more comparisons are in Supplement Section [16].

A. Runtime Analysis

We compare the running time of our approach with other state-of-the-art approaches. For the experiments, we use an NVIDIA RTX A5000 GPU and an Intel Xeon(R) W-2255 CPU. The average running time of our method includes 5 parts: 1. Point processing takes 0.5s with CPU or 0.2s with CUDA; 2. Voxel feature processing costs 0.03s; 3. Point feature processing takes 0.001s; 4. Registration takes 0.016s. We can observe a computational bottleneck in the point preprocessing step, as we have to get neighbors of the points and voxels in 5-stage voxelization. We can accelerate it using CUDA and the dynamic voxelization method [27].

Table I shows the comparisons with different state-of-the-art methods. Our approach has the running time comparable to these other approaches.

B. Overlap Estimation

We compare the overlap values directly from Geometric Transformer [15], Ground truth, and our approach. The LCDNet [10] is not here because it is trained with some positive/negative overlapped cases, not distances. The overlap values of the two point clouds are calculated by Equation 3. Also, as the Geometric Transformer is not able to directly estimate the overlap values of two point clouds, we took the exponential negative feature distances as the overlap values $o_{i,j}$ of voxels pairs, and the ground-truth voxel overlap values $o_{i,j}$ are computed by Equation 4. For our approach, the voxel overlap values $o_{i,j}$ are directly computed from the overlap estimation we presented before, and the overlap of the two point clouds is also calculated by 3.

From Figure 4, we can see that the overlap values of Geometric Transformer [15] cannot be used for overlap detection. In contrast, the overlap values from our model

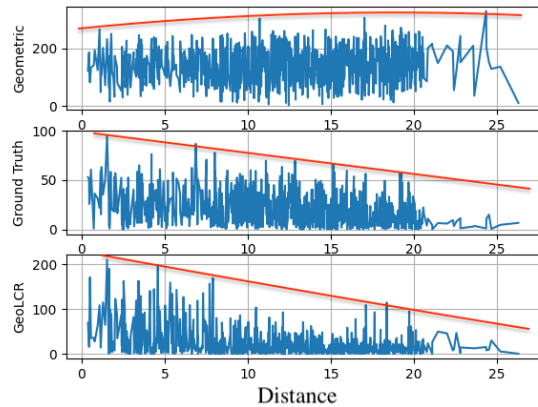


Fig. 4: Overlap Estimation: The sub-figures are overlap results tested in KITTI Sequence 7 with Geometric Transformer [15] (Top), Ground Truth transformations (Middle), and our approach (Bottom). The orange curves sketch the trend of the three curves. With the distance increasing, our approach is very effective for estimating the overlap values of the point clouds. It is also easy to choose a threshold value to the overlapping score for loop closure detection.

align well with the distance between two point clouds. Therefore, we can easily use it for loop closure estimation by giving a threshold to the overlap values.

C. Pose Estimation

To demonstrate the accuracy of the prediction of transformation matrices, we trained and evaluated our model by the metrics of LCD-Net [10] in KITTI and KITTI-360 datasets. We trained the model in Sequences [1,2,3,4,5,6,7,9,10] of KITTI and [0,3,4,5,6,7,10] of KITTI-360. Then we evaluated Sequences [0,8] of KITTI and [2,9] of KITTI-360. Because the KITTI ground truth transformation matrices are not very accurate, we used ICP to fine tune the ground truth matrices for the training and evaluation.

We compared our registration transformer’s performance with other algorithms. Since this module is used for loop closure frames, we have to temporarily select the distant frames that closely overlap. To that end, we used the same criteria as LCDNet [10] to make a fair comparison with the other algorithms. To be specific, as the metric in Algorithm 1 suggests, we select the loop closed frames only when the frame is not in the trajectory of the previous $10m$ distance but within $3m$ from the current key frame.

In Tables II and III, we present pose estimation errors for two sequences in each of the datasets. the translation error (TE) is calculated by the Euclidean distance between XYZ positions of the two frames. The rotation error (RE) is calculated as:

$$RE = \arccos \frac{\text{trace}(\hat{R}^T R_{\text{gt}}) - 1.0}{2}$$

	Seq. 00			Seq. 08		
	Success	TE (m) (succ. / all)	RE (deg) (succ. / all)	Success	TE (m) (succ. / all)	RE (deg) (succ. / all)
OverlapNet [9]	83.86%	- / -	1.28 / 3.89	0.10%	- / -	2.03 / 65.45
RPMNet [32]	47.31%	1.05 / 2.07	0.60 / 1.88	27.80%	1.28 / 2.42	1.77 / 13.13
DCP [30]	50.71%	0.98 / 1.83	1.14 / 6.61	0%	- / 4.01	- / 161.24
PCAM [33]	99.68%	0.07 / 0.08 ¹	0.35 / 0.74	94.90%	0.19 / 0.41	0.51 / 6.01
LCDNet [10]	100%	0.11 / 0.11	0.12 / 0.12	100%	0.15 / 0.15	0.34 / 0.34
LCDNet [†]	100%	0.14 / 0.14	0.14 / 0.14	100%	0.18 / 0.18	0.36 / 0.36
Ours (GeoLCR)	100%	0.06 / 0.06	0.33 / 0.33	100%	0.11 / 0.11	0.47 / 0.47

TABLE II: **Pose estimation error for positive pairs in the KITTI dataset.** In both sequences, our approach achieves better performance in translation accuracy and comparable rotation accuracy. In both cases, our method succeeded in detecting all the loop closure frames.

	Seq. 02			Seq. 09		
	Success	TE (m) (succ. / all)	RE (deg) (succ. / all)	Success	TE (m) (succ. / all)	RE (deg) (succ. / all)
OverlapNet	11.42%	- / -	1.79 / 76.74	54.33%	- / -	1.38 / 33.62
RPMNet	37.99%	1.18 / 2.26	1.30 / 5.97	41.42%	1.13 / 2.21	1.02 / 3.95
DCP	5.62%	1.09 / 3.14	1.36 / 149.27	30.10%	1.04 / 2.30	1.06 / 64.86
PCAM	97.46%	0.20 / 0.30	0.75 / 1.36	99.78%	0.12 / 0.13	0.51 / 0.64
LCDNet	98.62%	0.28 / 0.32	0.32 / 0.35	100%	0.18 / 0.18	0.20 / 0.20
LCDNet [†]	98.55%	0.27 / 0.32	0.32 / 0.34	100%	0.20 / 0.20	0.22 / 0.22
Ours (GeoLCR)	100%	0.08 / 0.08	0.35 / 0.35	100%	0.08 / 0.08	0.26 / 0.26

TABLE III: **Pose estimation error for positive pairs in the KITTI-360 dataset.** For both of the two sequences in the KITTI-360, our method achieved far better result in estimating translation. On both Sequence 02 and 09, our method estimates poses up to **two times better** than other algorithms in translation and shows comparable results in rotation. Also, our method succeeded in detecting loop closures for both the sequences (i.e. 100% success rate), while every other method failed on Sequence 02.

where \hat{R} is the estimated rotation matrix and R_{gt} is the ground truth rotation matrix. We compare the accuracy with LCDNet [10] and other recent methods. The [†] sign of LCDNet is to indicate that it has been trained on the KITTI-360 dataset. Otherwise, it is trained on the KITTI dataset, as mentioned in the LCDNet paper [10].

In Tables II and III, we can observe that our method achieves best results in translation estimation and comparable results in rotation estimation. Compared to other methods, our approach has at least a 30% improvement in translation estimation.

D. SLAM Trajectory

For the whole trajectory, we compare our approach with GICP [13]. For more comparisons please refer to the supplement material [16]. The key frames of the loop closure models are chosen from they frames published by Lio-sam odometry as Algorithm 1.

For the loop detection by GICP, we use it to process the transformation matrices between the current key frame and the selected historic key frames from Algorithm 1. Then if the distance is within the threshold of d_{th} in Algorithm 1, we assume there is a closed loop. Figure 5 shows the results in the KITTI Dataset Sequence 05, and we can observe that our approach (Blue) achieves better results compared to GICP (Red), especially when compared to the ground truth.

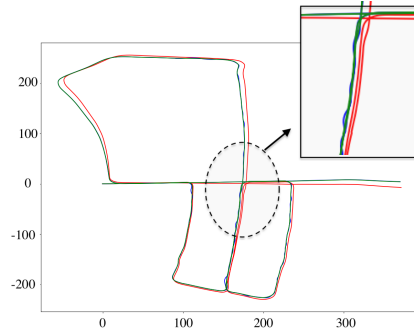


Fig. 5: The x and y axes are all meters. This figure shows the result of GeoLCR (Blue) compared with GICP (Red) and the ground truth (Green) trajectories. Because our method provides more accurate transformation matrices and loop closed detection, our approach achieves 0.26m error of the trajectory less than the 83.6m by GICP in Sequence 05 of the KITTI dataset.

V. LIMITATIONS, CONCLUSIONS, AND FUTURE WORK

We present a new learning pipeline, GeoLCR, for loop closure detection and points registration. We compare the accuracy of GeoLCR with LCDNet, OverlapNet, and other approaches in both KITTI and KITTI-360 datasets for points registration. Our method achieves up to **two times** improvements in terms of translation accuracy, and we also achieve comparable rotation accuracy. We compare the map results by genrating loop closure

constraints by GICP and achieve better accuracy w.r.t. the ground truth trajectory.

Our approach has some limitations. First, our current formulation is only designed for using the 3D Lidar as the perception sensor. In practice, Lidar can be sensitive to rainy or foggy weather. In future work, RGB data can help to improve the robustness of the system. Second, in this work, we use voxels to remove redundant points, but the method still uses many points for registration. In the future, we can choose points directly from the point level for registration.

REFERENCES

- [1] A. Geiger, P. Lenz, and R. Urtasun, "Are we ready for autonomous driving? the kitti vision benchmark suite," in *Conference on Computer Vision and Pattern Recognition (CVPR)*, 2012.
- [2] Y. Liao, J. Xie, and A. Geiger, "Kitti-360: A novel dataset and benchmarks for urban scene understanding in 2d and 3d," *IEEE Transactions on Pattern Analysis and Machine Intelligence*, 2022.
- [3] H. Caesar, V. Bankiti, A. H. Lang, S. Vora, V. E. Liong, Q. Xu, A. Krishnan, Y. Pan, G. Baldan, and O. Beijbom, "nusenes: A multimodal dataset for autonomous driving," in *Proceedings of the IEEE/CVF conference on computer vision and pattern recognition*, 2020, pp. 11 621–11 631.
- [4] J. Jeong, Y. Cho, Y.-S. Shin, H. Roh, and A. Kim, "Complex urban dataset with multi-level sensors from highly diverse urban environments," *The International Journal of Robotics Research*, vol. 38, no. 6, pp. 642–657, 2019.
- [5] N. Carlevaris-Bianco, A. K. Ushani, and R. M. Eustice, "University of michigan north campus long-term vision and lidar dataset," *The International Journal of Robotics Research*, vol. 35, no. 9, pp. 1023–1035, 2016.
- [6] G. Kim, Y. S. Park, Y. Cho, J. Jeong, and A. Kim, "Mulran: Multimodal range dataset for urban place recognition," in *2020 IEEE International Conference on Robotics and Automation (ICRA)*. IEEE, 2020, pp. 6246–6253.
- [7] W. Xu and F. Zhang, "Fast-lio: A fast, robust lidar-inertial odometry package by tightly-coupled iterated kalman filter," *IEEE Robotics and Automation Letters*, vol. 6, no. 2, pp. 3317–3324, 2021.
- [8] T. Shan and B. Englot, "Lego-loam: Lightweight and ground-optimized lidar odometry and mapping on variable terrain," in *2018 IEEE/RSJ International Conference on Intelligent Robots and Systems (IROS)*. IEEE, 2018, pp. 4758–4765.
- [9] X. Chen, T. Läbe, A. Milioto, T. Röhling, J. Behley, and C. Stachniss, "Overlapnet: a siamese network for computing lidar scan similarity with applications to loop closing and localization," *Autonomous Robots*, vol. 46, no. 1, pp. 61–81, 2022.
- [10] D. Cattaneo, M. Vaghi, and A. Valada, "Lcdnet: Deep loop closure detection and point cloud registration for lidar slam," *IEEE Transactions on Robotics*, 2022.
- [11] R. Mur-Artal, J. M. M. Montiel, and J. D. Tardos, "Orb-slam: a versatile and accurate monocular slam system," *IEEE transactions on robotics*, vol. 31, no. 5, pp. 1147–1163, 2015.
- [12] T. Shan, B. Englot, D. Meyers, W. Wang, C. Ratti, and D. Rus, "Lio-sam: Tightly-coupled lidar inertial odometry via smoothing and mapping," in *2020 IEEE/RSJ International Conference on Intelligent Robots and Systems (IROS)*. IEEE, 2020, pp. 5135–5142.
- [13] A. Segal, D. Haehnel, and S. Thrun, "Generalized-icp," in *Robotics: science and systems*, vol. 2, no. 4. Seattle, WA, 2009, p. 435.
- [14] T. Whelan, S. Leutenegger, R. Salas-Moreno, B. Glocker, and A. Davison, "Elasticfusion: Dense slam without a pose graph," *Robotics: Science and Systems*, 2015.
- [15] Z. Qin, H. Yu, C. Wang, Y. Guo, Y. Peng, and K. Xu, "Geometric transformer for fast and robust point cloud registration," in *Proceedings of the IEEE/CVF Conference on Computer Vision and Pattern Recognition*, 2022, pp. 11 143–11 152.
- [16] M. L. Jing Liang, Sanghyun Son and D. Manocha, "Geolcr: Attention-based geometric loop closure and registration." arXiv, 2023. [Online]. Available: <https://arxiv.org/pdf/2302.13509>
- [17] X. Zhang, L. Wang, and Y. Su, "Visual place recognition: A survey from deep learning perspective," *Pattern Recognition*, vol. 113, p. 107760, 2021.
- [18] P. Dellenbach, J.-E. Deschaud, B. Jacquet, and F. Goulette, "Ct-icp: Real-time elastic lidar odometry with loop closure," in *2022 International Conference on Robotics and Automation (ICRA)*. IEEE, 2022, pp. 5580–5586.
- [19] X. Ji, L. Zuo, C. Zhang, and Y. Liu, "Lloam: Lidar odometry and mapping with loop-closure detection based correction," in *2019 IEEE International Conference on Mechatronics and Automation (ICMA)*. IEEE, 2019, pp. 2475–2480.
- [20] X. Gao, R. Wang, N. Demmel, and D. Cremers, "Ldso: Direct sparse odometry with loop closure," in *2018 IEEE/RSJ International Conference on Intelligent Robots and Systems (IROS)*. IEEE, 2018, pp. 2198–2204.
- [21] S. Lin, J. Wang, M. Xu, H. Zhao, and Z. Chen, "Topology aware object-level semantic mapping towards more robust loop closure," *IEEE Robotics and Automation Letters*, vol. 6, no. 4, pp. 7041–7048, 2021.
- [22] L. Li, X. Kong, X. Zhao, W. Li, F. Wen, H. Zhang, and Y. Liu, "Sa-loam: Semantic-aided lidar slam with loop closure," in *2021 IEEE International Conference on Robotics and Automation (ICRA)*. IEEE, 2021, pp. 7627–7634.
- [23] Y. Zhou, Y. Wang, F. Poiesi, Q. Qin, and Y. Wan, "Loop closure detection using local 3d deep descriptors," *IEEE Robotics and Automation Letters*, vol. 7, no. 3, pp. 6335–6342, 2022.
- [24] Z. Zhou, C. Zhao, D. Adolfsson, S. Su, Y. Gao, T. Duckett, and L. Sun, "Ndt-transformer: Large-scale 3d point cloud localisation using the normal distribution transform representation," in *2021 IEEE International Conference on Robotics and Automation (ICRA)*. IEEE, 2021, pp. 5654–5660.
- [25] J. Ma, J. Zhang, J. Xu, R. Ai, W. Gu, and X. Chen, "Overlaptransformer: An efficient and yaw-angle-invariant transformer network for lidar-based place recognition," *IEEE Robotics and Automation Letters*, vol. 7, no. 3, pp. 6958–6965, 2022.
- [26] H. Thomas, C. R. Qi, J.-E. Deschaud, B. Marcotegui, F. Goulette, and L. J. Guibas, "Kpconv: Flexible and deformable convolution for point clouds," in *Proceedings of the IEEE/CVF international conference on computer vision*, 2019, pp. 6411–6420.
- [27] Y. Zhou, P. Sun, Y. Zhang, D. Anguelov, J. Gao, T. Ouyang, J. Guo, J. Ngiam, and V. Vasudevan, "End-to-end multi-view fusion for 3d object detection in lidar point clouds," in *Conference on Robot Learning*. PMLR, 2020, pp. 923–932.
- [28] H.-H. Chen, "Weighted-svd: Matrix factorization with weights on the latent factors," *arXiv preprint arXiv:1710.00482*, 2017.
- [29] A. Vaswani, N. Shazeer, N. Parmar, J. Uszkoreit, L. Jones, A. N. Gomez, L. Kaiser, and I. Polosukhin, "Attention is all you need," *Advances in neural information processing systems*, vol. 30, 2017.
- [30] Y. Wang and J. M. Solomon, "Deep closest point: Learning representations for point cloud registration," in *Proceedings of the IEEE/CVF international conference on computer vision*, 2019, pp. 3523–3532.
- [31] F. Dellaert, "Factor graphs and gtsam: A hands-on introduction," Georgia Institute of Technology, Tech. Rep., 2012.
- [32] Z. J. Yew and G. H. Lee, "Rpm-net: Robust point matching using learned features," in *Proceedings of the IEEE/CVF conference on computer vision and pattern recognition*, 2020, pp. 11 824–11 833.
- [33] A.-Q. Cao, G. Puy, A. Boulch, and R. Marlet, "Pcam: Product of cross-attention matrices for rigid registration of point clouds," in *Proceedings of the IEEE/CVF International Conference on Computer Vision*, 2021, pp. 13 229–13 238.

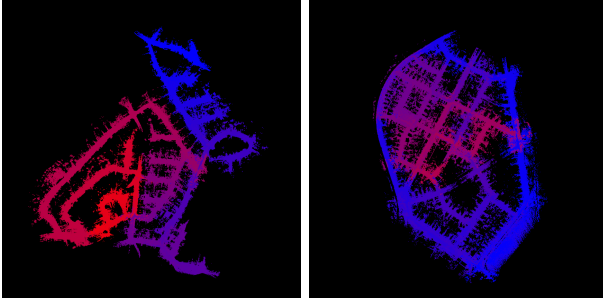


Fig. 6: Trajectory of Sequence 02 (left) and 09 (right) in the KITTI-360 dataset. The color coding indicates the starting point (Blue) and the end point (Red) of the moving vehicle. Note that loop closures occur at the points where two different colors overlap. Our method succeeded in detecting all of the loop closures in these sequences by using our novel point registration transformer, while other previous methods failed on these sequences.

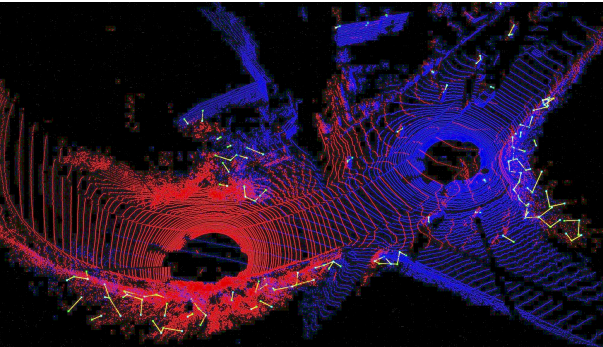


Fig. 7: An example of an overlapping area, where the red and blue points are from two different point clouds. The small green cubes are the centers of the voxels. The matched voxels are connected by the yellow lines. As shown, the matched voxels are mostly from the two sides of the road, which have more features than the road.

VI. SUPPLEMENT

A. Network Structures

In Figure 8, the inputs are points, \mathcal{P}_s and \mathcal{P}_k , from two key frames, s and k . After KPConv [26] feature encoder and Geometric Transformer [15], we process the features by 2 consecutive linear layers, and the details of the layers are mentioned in Section III-B. The outputs of the features are $N \times C$ and $M \times C$, respectively. Then we use Einstein sum to project the features to $N \times M \times C$ space. Then after post feature process, we project the two previous voxel features to the $N \times M \times C$ space again for more information about the voxel features themselves. The final output is the score map in the $N \times M$ space.

In Figure 9, we take advantage of the coarse features and project the point features to the voxel feature space.

After the normalization, we use two attention models to process the self relationship in each point cloud and cross relationship between two point clouds, then output the point features for point matching. The details of the Self-Attention and Cross-Attention models are mentioned in Section 3.3.

B. Comparisons with Other Datasets

In this section, we compare our method with LCD-Net [10] and Geometric Transformer [15] in NCLT, Complex Urban, and MulRan datasets in terms of registration errors. The errors are collected averagely among all loop-closed conditions in the sequence. From the tables IV and V, we can see our approach has a comparable results w.r.t. Geometric Transformer [15] and better results than GICP [13] and LCD-Net [10]. For the Table VI, the NCLT [5] dataset is collected from small robots with 16-channel Lidar, which has very sparse point and less number of points than other datasets. Therefore, all methods have bad performance in this datasets because there are some cases in open space with less features of the objects and in this condition all methods would perform bad. However, compared with other methods our method still achieved good average accuracy of both rotation and translation.

C. Comparisons with All Near Frames

We compared with LCD-Net [10] in other KITTI, KITTI-360, and Nuscenes datasets with not only loop closed cases, but all frame pairs with near distance. The table shows the results from all sequences from KITTI-360, Sequences 00 and 08 from KITTI datasets, and the results from the Nuscenes dataset. Compared with LCD-Net, our approach has a higher rate of nearby-frame detection and fewer translation and rotation errors. From Table VII-IX, we observe that our approach can detect all the near frames cases. Furthermore, our registration is more accurate than LCD-Net in both translation and rotation estimations.

For the two KITTI sequences in Table VII, we directly use the results from the table of LCD-NET. Our approach achieves comparable results w.r.t. translation and rotation errors.

For the KITTI-360 sequences, LCD-Net is tested by using the open-sourced pre-trained model. To achieve the best performance of LCD-Net, we also applied ground point removal according to the Github [10] command lines. Table VIII shows that our method is very robust in nearby frames detection, which is always 100% compared with the LCD-Net (around 50%). Our approach is also much more accurate in nearby-frame detection and can achieve much higher accuracy than LCD-Net in translation and rotation.

The Nuscenes dataset has more features than KITTI. There are more pedestrians, moving cars, and buildings

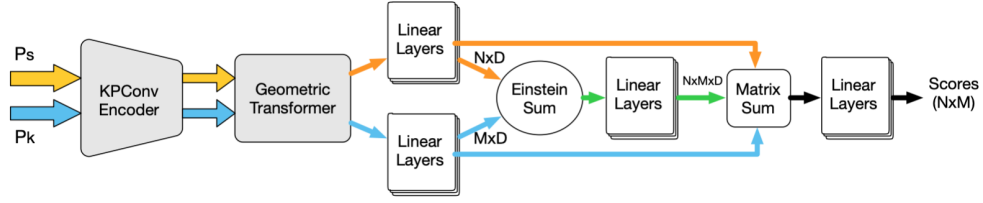


Fig. 8: Overlap Estimator: This is the network structure of the Overlap Estimator, which is composed of a KPCov encoder, Geometric Transformer, and Overlap Model.

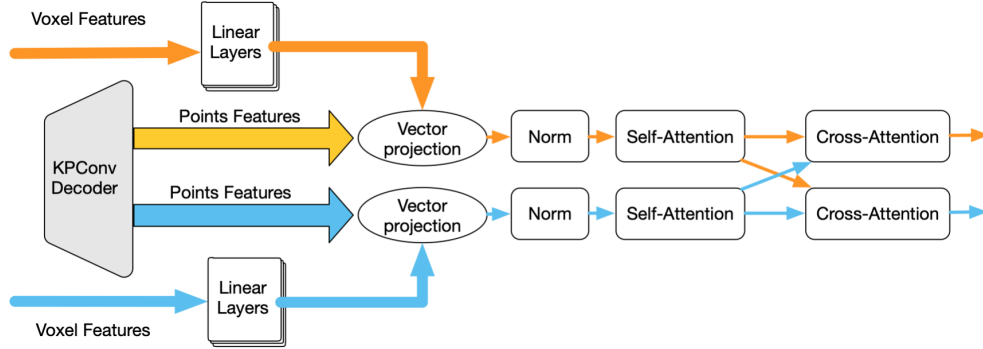


Fig. 9: Register: This is the network structure of the transformer model of the registration process. It takes the voxel features and point features and process the features by the attention models.

than in the scenarios in KITTI or KITTI-360. we collect the nearby-frame pair using a similar method and test the

Mulran [6]	Sejong01		Sejong02		Sejong03	
	TE (m)	RE (deg)	TE (m)	RE (deg)	TE (m)	RE (deg)
Ours (GeoLCR)	0.47	0.78	0.44	0.73	0.74	1.12
LCDNet [10]	5.44	20.81	4.42	16.57	5.26	19.59
Geometric Transformer [15]	0.14	0.38	0.15	0.42	0.41	0.30
GICP [13]	0.89	0.86	1.02	0.33	1.64	1.07

TABLE IV: Pose estimation error in the Mulran dataset [6].

Complex Urban [4]	Urban07		Urban08	
	TE (m)	RE (deg)	TE (m)	RE (deg)
Ours (GeoLCR)	0.71	3.12	0.65	2.50
LCDNet [10]	4.18	54.92	3.64	37.84
Geometric Transformer [15]	0.87	6.61	1.28	8.97
GICP [13]	2.13	83.23	1.44	29.00

TABLE V: Pose estimation error in the Complex Urban dataset.

NCLT [5]	2012-08-20		2012-10-28		2012-11-16	
	TE (m)	RE (deg)	TE (m)	RE (deg)	TE (m)	RE (deg)
Ours (GeoLCR)	1.24	10.1	1.63	15.1	1.64	13.9
LCDNet [10]	-	-	-	-	-	-
Geometric Transformer [15]	1.39	10.23	2.42	17.00	2.29	17.12
GICP [13]	4.17	128.98	4.05	107.83	3.37	86.69

TABLE VI: Pose estimation error in the NCLT dataset. Because the dataset is very sparse and there are not many points(16-channel Lidar), the LCD-Net failed in the dataset. For other methods, because there are some places in open space, there are not many features around the robot, all the algorithms perform bad in the situation, thus the average performance in NCLT dataset is generally worse than other datasets.

result with the dataset. From Table IX, we can see LCD-Net does not perform well in the nearby-frame situations in the Nuscenes dataset and the success rate is only 21%. However, our approach is still robust in the Nuscenes dataset with 100% success rate and accurate rotation and translation estimations.

	Ours (GeoLCR)			LCDNet [10]		
	Success	TE (m) (succ. / all)	RE (deg) (succ. / all)	Success	TE (m) (succ. / all)	RE (deg) (succ. / all)
KITTI Seq 00	100%	0.11 / 0.11	0.12 / 0.12	100%	0.14 / 0.14	0.13 / 0.13
KITTI Seq 08	100%	0.15 / 0.15	0.34 / 0.34	100%	0.19 / 0.19	0.24 / 0.24

¹ : We denote the best result with bold face.

TABLE VII: **Pose estimation error for positive pairs in the KITTI dataset.** Our method achieved a comparable result for translation and better performance for rotation.

	Ours (GeoLCR)			LCDNet [10]		
	Success	TE (m) (succ. / all)	RE (deg) (succ. / all)	Success	TE (m) (succ. / all)	RE (deg) (succ. / all)
KITTI-360 Seq 0	100%	0.14 / 0.14	0.13 / 0.13	44%	0.97 / 2.0	1.12 / 27.75
KITTI-360 Seq 2	100%	0.17 / 0.17	0.18 / 0.18	49.8%	1.00 / 1.93	1.37 / 14.98
KITTI-360 Seq 4	100%	0.16 / 0.16	0.15 / 0.15	44%	1.00 / 2.05	1.19 / 20.01
KITTI-360 Seq 5	100%	0.16 / 0.16	0.15 / 0.15	47%	0.97 / 2.03	1.39 / 22.1
KITTI-360 Seq 6	100%	0.17 / 0.17	0.15 / 0.15	57%	0.95 / 1.68	1.21 / 14.70
KITTI-360 Seq 9	100%	0.14 / 0.14	0.12 / 0.12	57%	0.92 / 1.54	1.13 / 9.82

¹ : We denote the best result with bold face.

TABLE VIII: **Pose estimation error for positive pairs in the KITTI-360 dataset.** Our approach achieves higher accuracy in rotation and translation estimations and more robust accuracy in nearby-frame detection.

Nuscenes	Success	TE (m) (succ. / all)	RE (deg) (succ. / all)
Ours (GeoLCR)	100%	0.15 / 0.15	0.12 / 0.12
LCDNet [10]	21%	0.57 / 11.59	1.91 / 20.95

¹ : We denote the best result with bold face.

TABLE IX: **Pose estimation error for positive pairs in the Nuscenes dataset.** The Nuscenes dataset, with more dynamic obstacles, is more complex than the KITTI or the KITTI-360. Our method achieved a comparable result for translation and better performance for rotation.